MSDE

PAPER

View Article Online
View Journal

Cite this: DOI: 10.1039/d5me00195a

Effect of the graft architecture of polymer-grafted nanoparticles on tribological behavior in polymer-brushed nanochannels

Taiga Morioka,[a] Yusei Kobayashi, *[ab] Takahiro Ikeda [abc] and Masashi Yamakawa[ab]

Although polymer brushes reduce friction by suppressing solid contact, performance degradation can occur under high shear and load. To address this, polymer-grafted nanoparticles (PGNPs) have been proposed as nanoscale spacers between wall brushes to stabilize the lubricating film and modulate the frictional response. In this study, dissipative particle dynamics were used to study PGNP solutions confined between polymer-brushed walls and relate self-assembly to the friction coefficient, μ, and shear viscosity, η. AB and BA diblock PGNPs (A: hydrophilic and B: hydrophobic) are compared with Janus architectures while varying the wall brush affinity from hydrophilic to hydrophobic. For hydrophilic wall brushes, AB-type PGNPs dimerized at equilibrium, whereas BA- and Janus-type PGNPs remained dispersed. Under shear, the viscosity exhibited shear-thinning, and architectural differences were minimal due to the dominance of wall brush alignment. Consequently, the tribological properties were similar across all PGNPs. For hydrophobic wall brushes, the PGNP architecture more strongly influenced self-assembly. At rest, AB-type PGNPs formed network-like aggregates, while BA-type and Janus PGNPs remained dispersed. Janus-type PGNPs preserved a solvent-rich core, yielding the lowest μ and η. At intermediate shear, BA-type PGNPs became less viscous than the Janus-type due to their low abundance in the channel center, reopening a low-resistance core pathway. The Janus-type PGNPs appeared in the channel center, which narrowed the solvent-rich core. At high shear, both architectures reconcentrated toward the center, and the differences in μ and η diminished. This work reveals how nanoscale self-assembly governs macroscopic tribological responses, offering design principles for next-generation PGNP-based lubricants.

Received 29th October 2025,
Accepted 23rd January 2026

DOI: 10.1039/d5me00195a

rsc.li/molecular-engineering

Design, System, Application

Polymer-grafted nanoparticles (PGNPs) are positioned as "programmable building blocks" that can freely control self-assembly tuned through molecular design. Furthermore, PGNPs function as a nanoscale bearing, reducing friction between polymer brush walls. We present design principles for systematically controlling the hydrophilic/hydrophobic balance, interfacial affinity, and brush–NP interactions under confinement by varying graft architectures, including diblock (AB- and BA-type) and Janus structures. These nanoscale design elements provide a guideline for directing self-assembly and optimizing tribological properties in lubricating nanolayers. Using dissipative particle dynamics simulations, we quantified the nanoscale friction and viscosity in the shear flow of PGNP solutions confined between hydrophilic and hydrophobic polymer-brush walls. Under hydrophilic conditions, wall-brush alignment dominated, resulting in minimal differences among architectures. Under hydrophobic conditions, architecture-dependent self-assembly emerged: AB-type PGNPs formed networks, while BA and Janus types remained dispersed, yet distinct spatial distributions caused a shear-induced viscosity crossover. These findings establish a mechanistic link between molecular design and tribology properties, providing guidelines for rational design of next-generation nanolubricants. The framework also extends to confined soft-matter systems, such as precision components, biomimetic bearings, and micro- or nanofluidic devices, where controlled self-organization and flow alignment govern macroscopic functionality.

1 Introduction

Polymer brushes are dense assemblies of polymer chains tethered onto solid substrates. When two brush-coated surfaces meet, a fluid layer forms and direct solid-to-solid contact is suppressed, thereby reducing friction and wear, and often producing shear thinning. These features enable the application of polymer brushes in precision components,

[a] Faculty of Mechanical Engineering, Kyoto Institute of Technology, Matsugasaki, Sakyo-ku, Kyoto 606-8585, Japan. E-mail: kobayashi@kit.ac.jp
[b] High-Performance Simulation Research Center, Kyoto Institute of Technology, Matsugasaki, Sakyo-ku, 606-8585, Kyoto, Japan
[c] Center for the Possible Futures, Kyoto Institute of Technology, Matsugasaki, Sakyo-ku, 606-8585, Kyoto, Japan

biomimetic bearings, and micro- or nanofluidic devices.[1–4] Despite these advantages, the performances of polymer brushes can deteriorate under demanding conditions. Specifically, at high shear rates or under large normal loads, the polymer chains can stretch, degrade, or detach from the surface, undermining both lubrication and the mechanical integrity.[5–8]

To address this issue, polymer-grafted nanoparticles (PGNPs) placed between opposing brushes have been proposed. In such systems, the PGNPs function as nanoscale spacers that limit interpenetration, redistribute stress, and stabilize the fluid film under flow.[9–11] Because the tribological response of these hybrid interfaces depends not only on the component properties but also on the self-assembled structure under confinement, establishing a quantitative link between the morphology and tribological properties is essential for rational design.

Through careful NP design, it is possible to treat particles as programmable building blocks, wherein their interactions are encoded by the surface chemistry, topology, and patch symmetry. Key interfacial properties, such as the brush softness, wettability contrast, and directionality can be controlled by adjusting the grafting density, block sequence, and patch geometry. These choices direct self-assembly across multiple length scales, enabling structures to be programmed with specific functions in mind. Foundational studies into block copolymers and NP composites have shown that compatibilization and symmetry determine the resulting mesophases and particle placement.[12–16] PGNPs, including patchy and Janus architectures, extend this concept and enable the formation of superlattices, finite clusters, and hierarchical frameworks that cannot be accessed using bare particles.[17–21] Soft brushes introduce a dual-length scale consisting of a rigid core and a programmable shell, which opens the design space for interfacial activity and selective adsorption at soft or liquid interfaces.[22–26] Asymmetric grafting and the use of sequence-programmed ligands, including DNA and amphiphiles, have also broadened the design space.[27–30] From the perspective of such building blocks, the particle architecture can be tailored to program both self-assembly and function.

Confinement reshapes the patterns by which these building blocks are assembled. In brushed nanochannels, spatial restrictions and wall interactions steer the layered, chain-like, or networked organization of PGNPs, with strong consequences for flow resistance and dissipation.[31–35] In our recent study into PGNP solutions confined between polymer-brushed walls, the solvent quality, grafting density, set dispersion, aggregation, and shear response were investigated. Under good solvent conditions, the particles remained dispersed, and shear-thinning behavior emerged with minimal sensitivity to the grafting density, wherein the wall-brush alignment dominated the response. Under poor-solvent conditions, the particles formed aggregates, and the friction and viscosity curves exhibited three regimes as the shear rate increased, namely aggregate growth, onset of breakup, and complete dispersion. Additionally, it was confirmed that stronger confinement promoted the flow alignment of the clusters and shifted the regimes. These guidelines provide a baseline for controlling friction and viscosity, and suggest that the surface architecture and explicit wall-to-polymer affinity are decisive levers that remain underexplored. However, the interplay between regime shifts and confinement is challenging to capture experimentally, especially under nanoconfinement and nonequilibrium shear. Consequently, a mesoscale simulation approach was considered.

Thus, in the current study, our previous work[46] is extended beyond homopolymer brushes to the design of graft architectures. Specifically, a graft polymer is programmed to form diblock brushes (AB and BA, where A is a hydrophilic segment and B is a hydrophobic segment) and Janus configurations. Under confinement, these designs are expected to yield more complex self-assembled structures, wherein the resulting morphological changes could translate into measurable differences in the tribological properties.[36,37] Additionally, the interactions of the wall-brushes are tuned from hydrophilic to hydrophobic to probe the coupling between the architecture and the wall. Furthermore, using the dissipative particle dynamics (DPD) method, the density redistribution across the slit and the orientational order of the particles and brushes are related to the friction coefficient and shear viscosity over a broad range of shear rates.

2 Methods and model

2.1 Dissipative particle dynamics (DPD) method

DPD is a particle-based mesoscopic simulation technique that was originally introduced by Hoogerbrugge and Koelman[38] and was subsequently refined by Español and Warren.[39,40] In DPD simulations, a DPD bead represents a group of atoms or molecules, enabling longer simulation times and the exploration of larger spatial scales compared with classical molecular dynamics simulations. As one of the most powerful mesoscopic simulation tools, the DPD method has been applied to numerous self-assembling systems with polymer brushes, including confined liquids.[9,31–33,41–44] The DPD method is governed by Newton's equations of motion, wherein each DPD bead is subjected to three types of intermolecular forces, namely conservative, dissipative, and random. Newton's equation of motion for a particle i is expressed as follows:

$$m_i \frac{\mathrm{d}v_i}{\mathrm{d}t} = f_i = \sum_{j \neq i} F_{ij}^{\mathrm{C}} + \sum_{j \neq i} F_{ij}^{\mathrm{D}} + \sum_{j \neq i} F_{ij}^{\mathrm{R}}, \quad (1)$$

where m is the mass, v is the velocity, F^{C} is the conservative force, F^{D} is the dissipative force, and F^{R} is the pairwise random force. The sum of the forces acting on all beads between particles i and j is calculated. The conservative force is softly repulsive and is given by

$$F_{ij}^{C} = \begin{cases} a_{ij}\left(1-\frac{|r_{ij}|}{r_c}\right)n_{ij}, & |r_{ij}| \le r_c \\ 0, & |r_{ij}| > r_c \end{cases}, \quad (2)$$

where $r_{ij} = r_j - r_i$ and $n_{ij} = r_{ij}/|r_{ij}|$. a_{ij} describes the magnitude of the repulsive force between beads i and j, while r_c is the cutoff distance. The dissipative force F_{ij}^{D} and random force F_{ij}^{R} can be expressed as follows:

$$F_{ij}^{D} = \begin{cases} -\gamma\omega^{D}(|r_{ij}|)(n_{ij}\cdot v_{ij})n_{ij}, & |r_{ij}| \le r_c \\ 0, & |r_{ij}| > r_c \end{cases} \quad (3)$$

and

$$F_{ij}^{R} = \begin{cases} \sigma\omega^{R}(|r_{ij}|)\zeta_{ij}\Delta t^{-1/2}n_{ij}, & |r_{ij}| \le r_c \\ 0, & |r_{ij}| > r_c \end{cases} \quad (4)$$

where $v_{ij} = v_j - v_i$, σ is the noise parameter, γ is the friction parameter, and ζ_{ij} is a random number based on a Gaussian distribution. Here, ω^{R} and ω^{D} are r-dependent weight functions that can be expressed as follows:

$$\omega^{D}(r) = [\omega^{R}(r)]^2 = \begin{cases} \left[1-\frac{|r_{ij}|}{r_c}\right]^2, & r_{ij} \le r_c \\ 0, & r_{ij} > r_c \end{cases}. \quad (5)$$

In this case, the temperature T is controlled by the balance between F_{ij}^{D} and F_{ij}^{R}. The values of σ and γ are related to one another by the fluctuation–dissipation theorem through the following equation:

$$\sigma^2 = 2\gamma k_B T, \quad (6)$$

where k_B denotes the Boltzmann constant. Notably, reduced units are often used in the DPD simulations. In this case, the length units represent the cutoff distance, r_c, the unit of mass is the bead mass m, the unit of energy is k_BT, and the time unit defined by $\tau = r_c(m/k_BT)^{1/2}$. The thermal energy is used as the energy scale and we set $k_BT = 1.0$ in reduced units.[45]

2.2 Models and conditions

The coarse-grained PGNP models and polymer-brushed walls employed herein were constructed based on previous studies.[46] Fig. 1(a–c) illustrate the coarse-grained models, wherein each NP is represented as a rigid body.[47] The radius of each NP, R_{NP}, was defined as $3.0\,r_c$, comprising 1684 DPD beads arranged on a diamond lattice with a lattice constant of $0.73\,r_c$ (ref. 32, 33 and 48) (Fig. 1(a)). The graft polymer comprising the NP or wall brushes is linear, with the nearest-neighbor particles connected by a harmonic spring force:

$$F_{ij}^{S} = -k(|r_{ij}| - r_s)n_{ij} \quad (7)$$

where $k = 150\,k_BT/r_c^2$ is the spring constant and $r_s = 0.85\,r_c$ is the equilibrium bond length. The chain lengths of the NP and the wall brushes were $M = 6$ and 18, respectively, where M represents the number of monomers in each grafted chain. The chain lengths considered here are relatively short. Accordingly, the present simulations are most relevant to unentangled brush systems, and the effects of entanglements are beyond the scope of this study. These parameters were inspired by a previous simulation of a single PGNP in solution confined within polymer-brushed walls, as reported by Nguyen *et al.*[9] Harmonic spring forces F_{ij}^{S} are also applied to the bonds connecting one end of the polymer bead to the NP or wall surface. As represented schematically in Fig. 1(b), three types of polymers were used to cover the NPs, namely a hydrophilic (labelled A) homopolymer with $M_A = M = 6$, a hydrophobic (labelled B) homopolymer with $M_B = M = 6$, and diblock copolymers with $M_A = 3$ and $M_B = 3$. As shown in Fig. 1(c), the PGNPs were constructed in three architectures: (i) an A–B diblock (AB), (ii) the same A–B diblock grafted with the opposite orientation (BA), and (iii) a Janus type where A and B homopolymers are grafted on opposite hemispheres.

The graft density $\Gamma = N_g/(2\pi R_{NP}^2)$ was set as $\Gamma = 0.77\,r_c^{-2}$ (87), where the numbers in parentheses indicate the corresponding values of N_g. Each wall (labelled W) has a

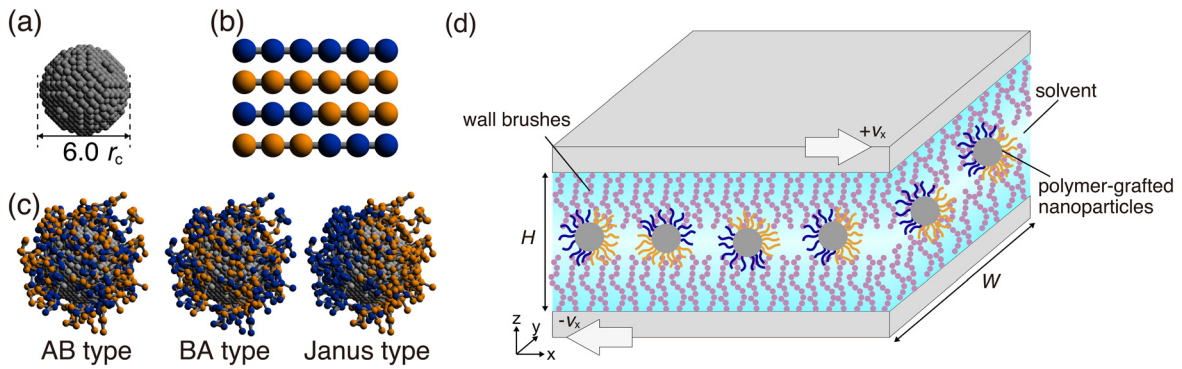

Fig. 1 (a) Nanoparticle (NP) with radius $R_{NP} = 3.0\,r_c$. (b) Schematic view of four types of NP brushes: a purely hydrophilic homopolymer, including a purely hydrophobic homopolymer, a hydrophilic–hydrophobic (denoted by AB type) diblock copolymer, and a hydrophobic–hydrophilic (denoted by BA type) diblock copolymer. (c) Polymer-grafted NPs (PGNPs) coated with AB-type diblock copolymers, BA-type diblock copolymers, and homopolymers forming a Janus surface. (d) Schematic representation of the PGNPs in solution confined within a nanochannel coated with polymer brushes.

surface area of $A = 50 \times 50\, r_c^2$ and is constructed from DPD beads arranged in a face-centered cubic lattice with a lattice constant of $0.5\, r_c$. The distance between the two (bare) wall surfaces was set to $H = 15\, r_c$. Two distinct types of wall-brushes were examined, namely hydrophilic (block A) and hydrophobic (block B) homopolymers. For the polymer-brushed walls, the graft density was fixed at $\Gamma_{wall} = 2.0\, r_c^{-2}$ (5000).[49,50] Grafting points were randomly distributed on the NP and wall surfaces, and the solvent was treated as a single bead.

The interaction parameters for F_{ij}^C were set between any two DPD particles a_{ij}, based on previous studies.[9,46] All interaction parameters are listed in Table 1. We fixed the self-interaction parameters at $a_{ii} = 30\, k_B T/r_c$ for all bead types, following common practice in DPD simulations and consistent with previous studies.[9,46] Here, the DPD fluid is treated as an effective coarse-grained solvent, and we focus on relative trends when varying the PGNP graft architecture and the affinity of the wall-grafted brushes. The NP core beads were treated as chemically neutral, *i.e.*, the conservative interaction parameters between NP beads and all other bead types (A, B, S, and W) were set to the self-interaction value ($a_{NP,j} = a_{ii}$). With the NP modeled as a rigid sphere composed of multiple DPD beads, geometric excluded-volume effects are already captured at the level of the core geometry. This modeling choice enables us to isolate the influence of grafted polymers and wall-grafted brushes on self-assembly and tribological response. The interaction contrasts that control hydrophilicity/hydrophobicity and A–B mixing were intentionally kept modest to represent a weakly amphiphilic system ($a_{ij} = 28\, k_B T/r_c$ or $32\, k_B T/r_c$ *vs.* $a_{ii} = 30\, k_B T/r_c$), consistent with previous DPD studies on related PGNP/brush systems.[9,46] Despite this modest contrast, the parameters are sufficient to induce equilibrium self-organization, such as dimerization/clustering of amphiphilic PGNPs and network-like aggregation under nanoconfinement.

A schematic illustration of a representative system is shown in Fig. 1(d). In the initial configuration, PGNPs and the solvent were randomly positioned within the confined system. In all simulations, the number of PGNPs was fixed at $N_{NP} = 16$. The PGNPs were confined between two polymer-brushed walls and the remaining system volume was filled with solvent beads to achieve a number density ρ of $4.0\, r_c^{-3}$. The total number of solvent beads was $N_S = 142\,761$. The temperature was set as $1.0\, k_B T$, while the noise parameter σ and friction parameter γ were set as 3.0 and 4.5, respectively. The time step dt was $0.04\,\tau$, and a periodic boundary condition was applied in the x- and y-directions.

Prior to shear flow application, equilibrium simulations were conducted under each condition for at least 2×10^6 steps. Shear simulations were subsequently performed once the potential energy reached a stable plateau. Although the systems may become trapped in metastable states that persist longer than the accessible simulation timescales, even in DPD simulations,[51] this criterion is commonly used to verify that a thermodynamic equilibrium has been reached. Shear flow was applied by imposing a constant sliding velocity $\pm V_x$ on the upper and lower walls (see Fig. 1(d)). The shear rate was defined as $\dot{\gamma} = 2V_x/H$. Additionally, the imposed sliding velocity, V_x, varied from $2.0 \times 10^{-2}\, r_c/\tau$ to $1.0\, r_c/\tau$, corresponding to an apparent shear rate in the range of $2.7 \times 10^{-3}\, \tau^{-1} \lesssim \dot{\gamma} \lesssim 1.3 \times 10^{-1}\, \tau^{-1}$. To characterize the shear conditions in a dimensionless manner, we evaluated a representative relaxation time, τ_R, of the hydrophilic wall-grafted polymers from equilibrium simulations. We computed the normalized autocorrelation function of the end-to-end vector of a wall-grafted chain, $\mathbf{R}_e(t)$, as

$$C_R(t) = \frac{\langle \mathbf{R}_e(t) \cdot \mathbf{R}_e(0) \rangle}{\langle \mathbf{R}_e(0) \cdot \mathbf{R}_e(0) \rangle}, \tag{8}$$

where $\langle \cdots \rangle$ denotes averaging over all wall-grafted chains and multiple time origins. We then determined τ_R by fitting $C_R(t)$ to a single-exponential form, $C_R(t) \sim \exp(-t/\tau_R)$, so that τ_R corresponds to the characteristic decay time (equivalently, the time at which $C_R(\tau_R) = e^{-1}$). Using this relaxation time, which was estimated as $\tau_R \approx 200\,\tau$, the Weissenberg number was defined as $W_i = \tau_R \dot{\gamma}$. For the shear-rate range investigated in this study, the corresponding Weissenberg number spans $0.5 \lesssim W_i \lesssim 26$.

The shear viscosity was determined by $\eta = \langle \sigma_{xz} \rangle / \dot{\gamma}$, where $\langle \cdots \rangle$ denotes the time average, and σ_{xz} represents the xz component of the stress tensor. The friction coefficient was defined as the ratio of shear stress to normal stress, given by $\mu = \langle \sigma_{xz} \rangle / \langle \sigma_{zz} \rangle$. All simulations were performed using GPU-accelerated versions[52] of the Large-scale Atomic/Molecular Massively Parallel Simulator (LAMMPS) package.[53]

Table 1 Interaction parameters, a_{ij}, in F_{ij}^C [see eqn (2)] between all pairs. All values[a] are given in units of $k_B T/r_c$

	NP	A	B	S	W
NP	30	30	30	30	30
A		30	32	28	30
B			30	32	30
S				30	30
W					0

[a] NP: nanoparticle, A: hydrophilic monomer, B: hydrophobic monomer, S: solvent, W: wall.

3 Results and discussion

Initially, the equilibrium morphologies of the amphiphilic PGNPs exhibiting different architectures were investigated. Fig. 2 shows representative snapshots of the PGNPs confined between the hydrophilic (panels (a–c)) and the hydrophobic wall-brushes (panels (d–f)). For the system employing hydrophilic brushes, the diblock AB-type PGNPs self-assembled into dimers, whereas the diblock BA- and Janus-type PGNPs remained well dispersed. Notably, the Janus-type PGNPs remain well dispersed under the hydrophilic brushes at equilibrium. This behavior is likely promoted by the strong confinement imposed by the dense hydrophilic wall brushes

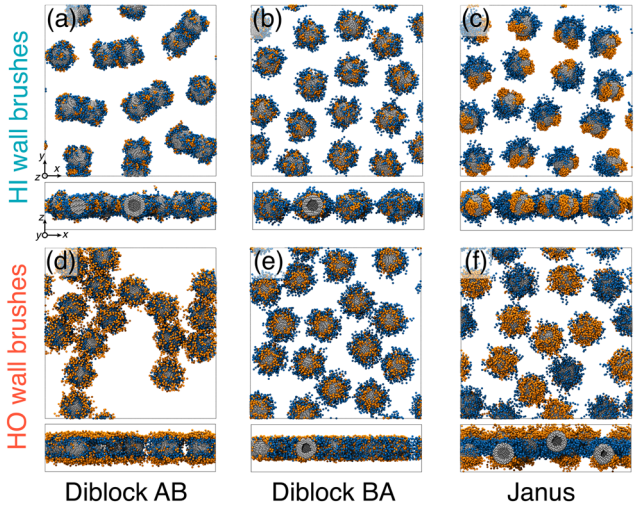

Fig. 2 Representative snapshots of equilibrium morphologies under (a–c) hydrophilic (HI) wall brushes and (d–f) hydrophobic (HO) wall brushes for the different grafting architectures of PGNPs, as indicated. For each case, the upper panel shows the top view and the lower panel shows the side view. Solvent beads and wall-grafted brush chains are omitted for clarity.

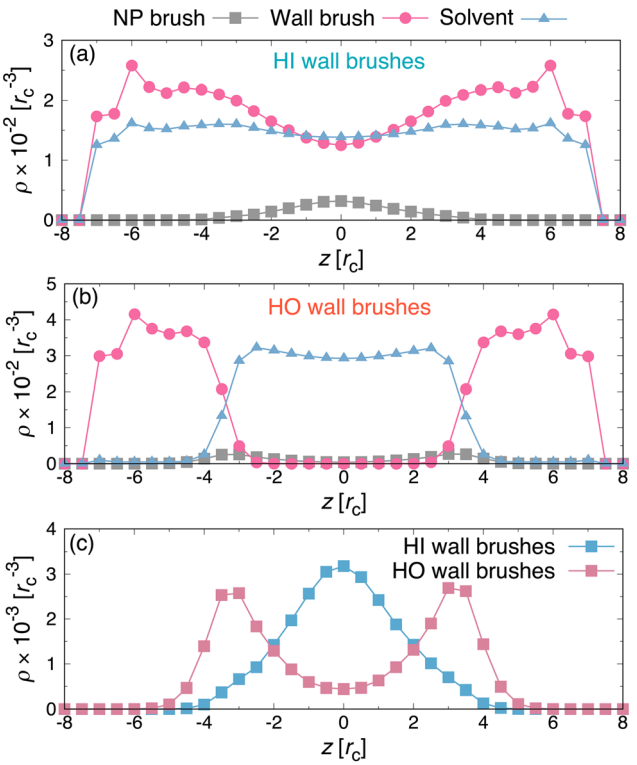

Fig. 3 Number density profiles of the confined NP brushes, solvent, and wall brushes along the wall-normal (z) direction for diblock AB-type PGNPs at equilibrium under (a) hydrophilic (HI) and (b) hydrophobic (HO) wall brushes. For clarity, panel (c) shows the NP number density profile alone for both cases.

and the resulting restriction of translational and rotational motions. In addition, the hydrophilic hemisphere (M_A = 6) tends to be more extended under hydrophilic conditions, which effectively increases the steric footprint of the particle and can hinder the approach and mutual reorientation of the B hemispheres required for fusion-like aggregation. A systematic assessment of how the wall-brush grafting density influences this aggregation behavior is left for future work. In the case of hydrophobic brushes, the diblock AB-type PGNPs tended to form large network-like aggregates, and an apparent wetting of the B domains of PGNPs was also observed (Fig. 2(d)). We believe that this wetting is promoted by the high grafting density of the wall brushes used in this study. At this grafting density, the hydrophobic wall brushes form a dense, B-rich layer near the walls. The B blocks of the AB-type PGNPs therefore preferentially contact this layer, and the PGNPs position themselves to maximize B(PGNP)–B(wall) contacts. The diblock BA-type PGNPs exhibited a comparable dispersion to that observed in the presence of hydrophilic brushes. Additionally, although the Janus-type PGNPs were also effectively dispersed, their hydrophobic hemispheres were in clear contact with the hydrophobic wall brushes.

To quantify the molecular distributions in these systems, the density profiles were computed for the polymers grafted on the diblock AB-type PGNPs, the wall brushes, and the solvent along the wall-normal direction (Fig. 3). Under the hydrophilic brush conditions (Fig. 3(a)), the density of the polymer grafted on the NPs exhibited a pronounced maximum at the center of the system ($z = 0\,r_c$). Similar distributions have been previously reported and are attributed to a reduction in the conformational entropy of the wall brushes upon the sequestration of NPs.[46,54,55] The solvent, which interacts favorably with both the NPs and the hydrophilic wall-brushes, remained essentially uniform throughout the slit, and the wall-brushes were correspondingly extended owing to their affinity for the solvent. In contrast, under hydrophobic wall brush conditions (Fig. 3(b)), the NP brushes did not accumulate at the center; instead, they were distributed within $-4\,r_c \lesssim z \lesssim -2\,r_c$ and $2\,r_c \lesssim z \lesssim 4\,r_c$. The solvent was enriched in the central region ($-4\,r_c \lesssim z \lesssim 4\,r_c$), avoiding contact with the outer hydrophobic blocks of the PGNPs and the wall-brushes, and was depleted near the walls. The wall-brushes contracted and became localized at the walls, with essentially negligible density in the central region. Although Fig. 3 shows only the results for the diblock AB-type PGNPs, qualitatively similar trends were observed for the BA- and Janus-type architectures (data not shown).

Following the equilibrium simulations, shear was applied to investigate the frictional response in the steady state. Fig. 4 shows representative snapshots of the sheared PGNPs confined between the hydrophilic wall brushes. For the diblock AB-type PGNPs, small aggregates aligned with the flow direction, while some aggregates coalesced into larger clusters as the shear rate $\dot{\gamma}$ was increased (Fig. 4(a) and (b)). At a high shear rate ($\dot{\gamma} = 1.3 \times 10^{-1}\,\tau^{-1}$), the aggregates were elongated in the flow direction, as shown in Fig. 4(c). For the diblock BA-type PGNPs, the dispersed state persisted at low shear rates, as under equilibrium conditions (*cf.*

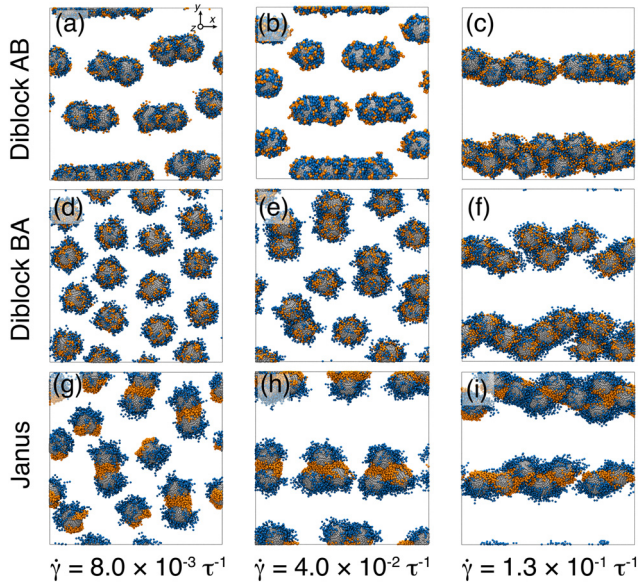

Fig. 4 Representative snapshots of steady-state morphologies under hydrophilic wall brushes for (a–c) diblock AB-type, (d–f) diblock BA-type, and (g–i) Janus-type PGNPs, and shear rates $\dot{\gamma}$, as indicated. For clarity, only the PGNPs are shown. Flow direction is along x and the velocity gradient is along z.

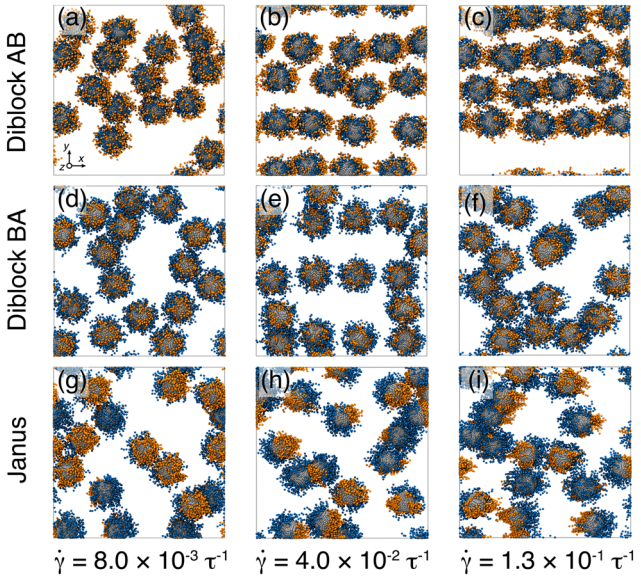

Fig. 5 Same as Fig. 4, but under hydrophobic wall brushes for (a–c) diblock AB-type, (d–f) diblock BA-type, (g–i) Janus-type PGNPs. Flow direction is along x and the velocity gradient is along z.

Fig. 2(b) and 4(d)). As the shear rate was increased, aggregation occurred and ultimately yielded flow-aligned structures similar to those observed for the AB-type PGNPs (Fig. 4(e) and (f)). For the Janus-type PGNPs, initial aggregate growth was observed at low shear rates (*cf.* Fig. 2(c) and 4(g)), as also observed for the AB-type PGNPs. Similar shear-induced aggregate growth has been reported in previous simulations of Janus colloidal suspensions[56] and Janus colloidal–polymer mixtures under dilute conditions.[57–59] Upon increasing $\dot{\gamma}$, the PGNPs self-assembled into trimers and eventually large flow-aligned aggregates were formed, as shown in Fig. 4(h) and (i). Fig. 5 shows representative snapshots of the sheared PGNPs confined between the hydrophobic wall brushes. Compared with the case of the hydrophilic wall-brushes, the differences in the self-assembled structures among the PGNP grafting architectures were more pronounced under hydrophobic wall-brush conditions. For the diblock AB-type PGNPs, large network-like aggregates persisted at low $\dot{\gamma}$ values (Fig. 5(a)) and flow-aligned clusters were formed as the shear rate was increased (Fig. 5(b) and (c)). The diblock BA-type PGNPs remained dispersed over the entire $\dot{\gamma}$ range (Fig. 5(d–f)), while the Janus-type PGNPs came into contact with the hydrophobic wall-brushes at low shear rates (Fig. 5(g)). Upon increasing $\dot{\gamma}$, the PGNPs were desorbed from the wall brushes, as shown in Fig. 5(h) and (i).

To further characterize the structural response of the wall-grafted polymer brushes under shear, we analyzed the orientational distribution $P(\cos\theta)$, where θ is the angle between the end-to-end vector of a grafted chain, $\mathbf{R}_e$, and the wall-normal direction $\mathbf{e}_z$ (Fig. 6). We found that the orientational behavior of the wall-grafted polymers showed no pronounced dependence on the PGNP architecture for either hydrophilic or hydrophobic wall brushes. Under hydrophilic wall conditions (-Fig. 6(a–c)), the grafted polymers were predominantly oriented normal to the wall ($\cos\theta \approx 1$) in equilibrium. With increasing shear rate, the fraction of vertically oriented chains decreased and the orientational distribution shifted toward smaller $\cos\theta$, indicating progressive tilting toward the flow direction. At high shear rates, an increased population was observed around $\cos\theta \approx 0.5$, indicating partial alignment toward the shear flow. In contrast, for hydrophobic wall conditions (Fig. 6(d–f)), vertical alignment remained dominant up to intermediate shear rates, whereas at high shear rates a clear peak emerged around $\cos\theta \approx 0.4$. These results indicate that shear flow induces a gradual reorientation of the wall-grafted polymers, while the overall orientational response is only weakly dependent on the PGNP architecture.

Fig. 7 shows the friction coefficient μ and shear viscosity η as functions of the shear rate $\dot{\gamma}$. For reference, we also performed simulations without PGNPs under otherwise identical conditions. The corresponding normalized friction coefficient and viscosity, $\mu_r = \mu/\mu_0$ and $\eta_r = \eta/\eta_0$, are provided in the SI (Fig. S1), where μ_0 and η_0 denote the values for the corresponding brush-only systems under each wall condition. Under hydrophilic wall-brush conditions, the friction coefficient μ increased with the shear rate $\dot{\gamma}$, whereas the shear viscosity η decreased, representing typical shear-thinning behavior (Fig. 7(a) and (b)). These trends are consistent with our previous simulation results obtained under good solvent conditions.[46] Furthermore, no significant differences in μ or η were observed across the different PGNP architectures. Taken together, these results indicate that in the presence of hydrophilic wall-brushes, the frictional μ and viscous η responses are dominated by wall-brush-mediated contributions rather than by self-assembled or dispersed

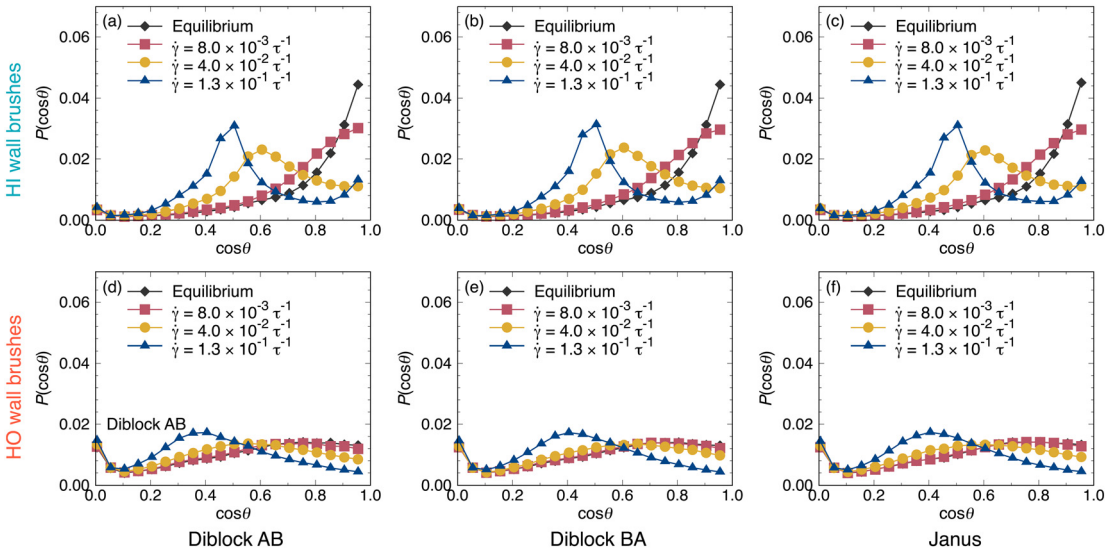

Fig. 6 Friction coefficient, μ, and shear viscosity, η, as functions of shear rate, $\dot{\gamma}$, under (a and b) hydrophilic wall brushes and (c and d) hydrophobic wall brushes for various grafting architectures of PGNPs, as indicated.

PGNP structures. In the presence of hydrophobic wall-brushes, both the friction coefficient μ and the shear viscosity η remained lower than those under hydrophilic wall-brush conditions, and the differences among the PGNP architectures were more pronounced. Specifically, for $1.3 \times 10^{-3}\,\tau^{-1} \lesssim \dot{\gamma} \lesssim 1.3 \times 10^{-2}\,\tau^{-1}$, the Janus-type PGNPs exhibited the lowest μ and η values. However, at $\dot{\gamma} \gtrsim 1.3 \times 10^{-2}\,\tau^{-1}$, the ordering of μ and η between the diblock BA and Janus architectures reversed, with the BA-type PGNPs exhibiting the lowest values. This crossover is discussed in detail below.

To rationalize the tribological behavior shown in Fig. 7, the density profiles were computed along the wall-normal direction for the solvent, the wall-brushes, and the polymers grafted onto the PGNPs (NP brushes), as shown in Fig. 8. In the presence of hydrophilic wall-brushes, increasing the shear rate $\dot{\gamma}$ led to a decrease in the wall-brush density in the central region (*i.e.*, $|z| \lesssim 2\,r_c$), whereas the densities of the NP brushes and the solvent increased in the same region. These behaviors arise from the shear-induced alignment of the wall-brushes along the flow direction, which is in near-quantitative agreement with previous simulations.[46,60]

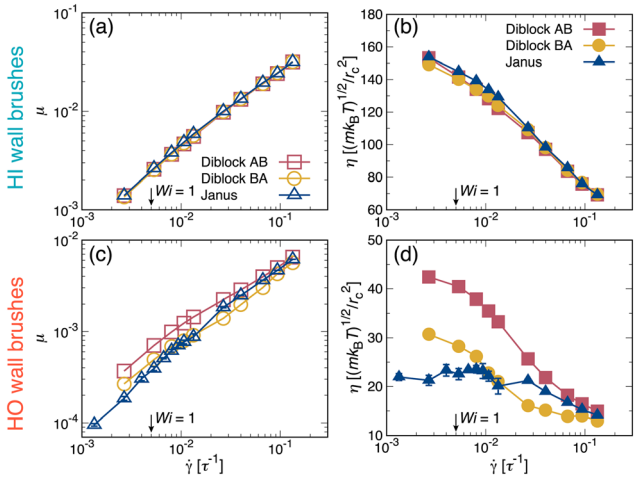

Fig. 7 Density profiles of confined NP brushes, solvent, and wall brushes along the wall-normal direction, under hydrophilic wall brushes for various grafting architectures of PGNPs, and shear rates $\dot{\gamma}$, as indicated.

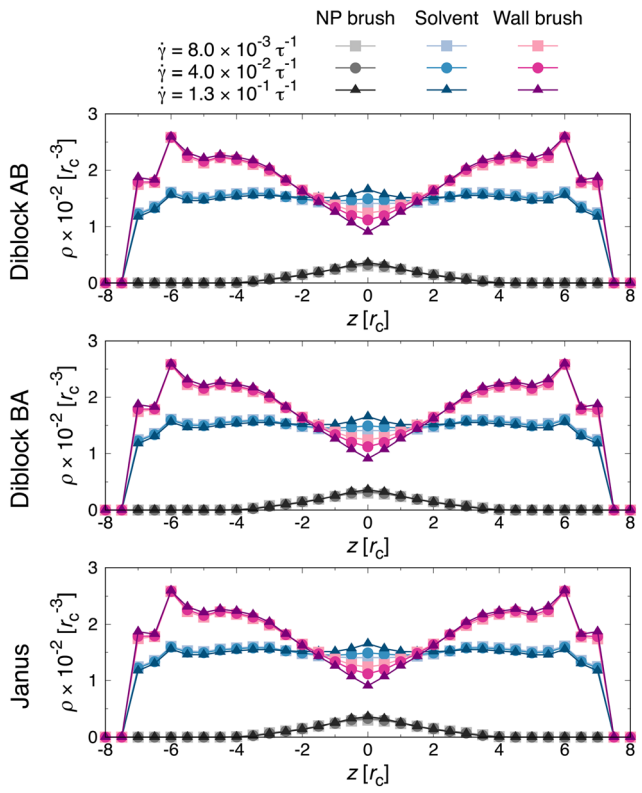

Fig. 8 Same as Fig. 7, but under hydrophobic wall brushes.

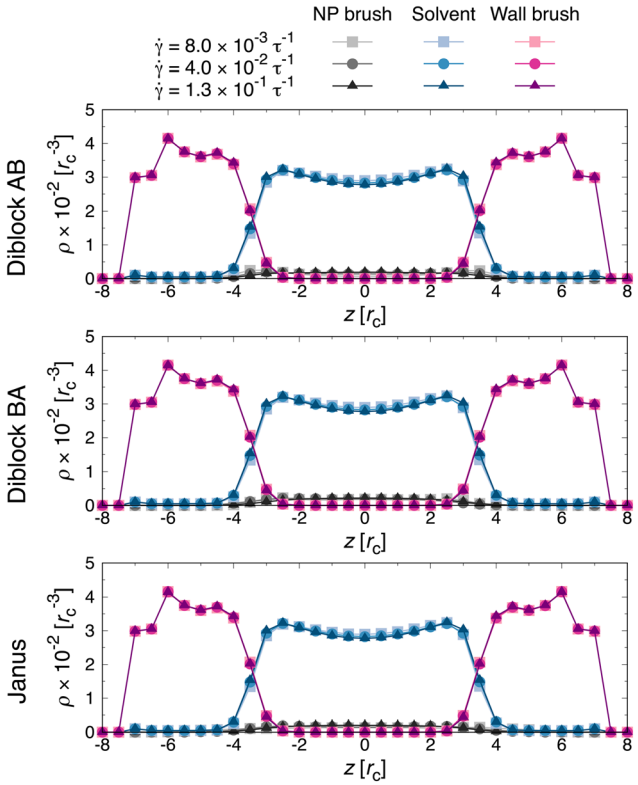

Fig. 9 Orientational distributions, $P(\cos\theta)$, of grafted polymer chains on PGNPs under (a–c) hydrophilic wall brushes and (d–f) hydrophobic wall brushes for various grafting architectures of PGNPs, and shear rates $\dot{\gamma}$, as indicated.

Importantly, the grafted architectures of the PGNPs (diblock AB, BA, and Janus) did not disrupt this alignment mechanism and their effects on the friction coefficient and viscosity were negligible under hydrophilic conditions. These results indicate that in the presence of hydrophilic wall-brushes, the flow behavior is governed primarily by wall-brush-mediated shear alignment rather than by the dispersed or self-assembled structures of the PGNPs.

Fig. 9 shows the density profiles of the hydrophobic wall brushes. As shown in Fig. 3, in the equilibrium state ($\dot{\gamma} = 0\,\tau^{-1}$), the system exhibits the characteristic segregation typical of hydrophobic wall brushes. Specifically, the wall-brush density was found to be strongly localized near the walls, the solvent was enriched at the central region (*i.e.*, $|z| \lesssim 4\,r_c$), and a peak corresponding to the NP brushes appeared at $|z| \approx 3\,r_c$, respectively. Upon increasing $\dot{\gamma}$, the wall-brush localization remained pronounced, the solvent peak at $|z| \approx 2\,r_c$ intensified slightly and narrowed, and the NP-brush peaks observed at $|z| \approx 3\,r_c$ shifted modestly toward a smaller $|z|$ and became broader. These changes reflect shear-induced redistribution within a solvent-rich central zone while maintaining strong brush–NP incompatibility near the walls.

To further investigate the shear-induced structural changes occurring in the PGNPs and determine their relationship with the tribological properties, Fig. 10 shows the density profiles of the NP centers-of-mass along the wall-normal direction, together with representative snapshots at

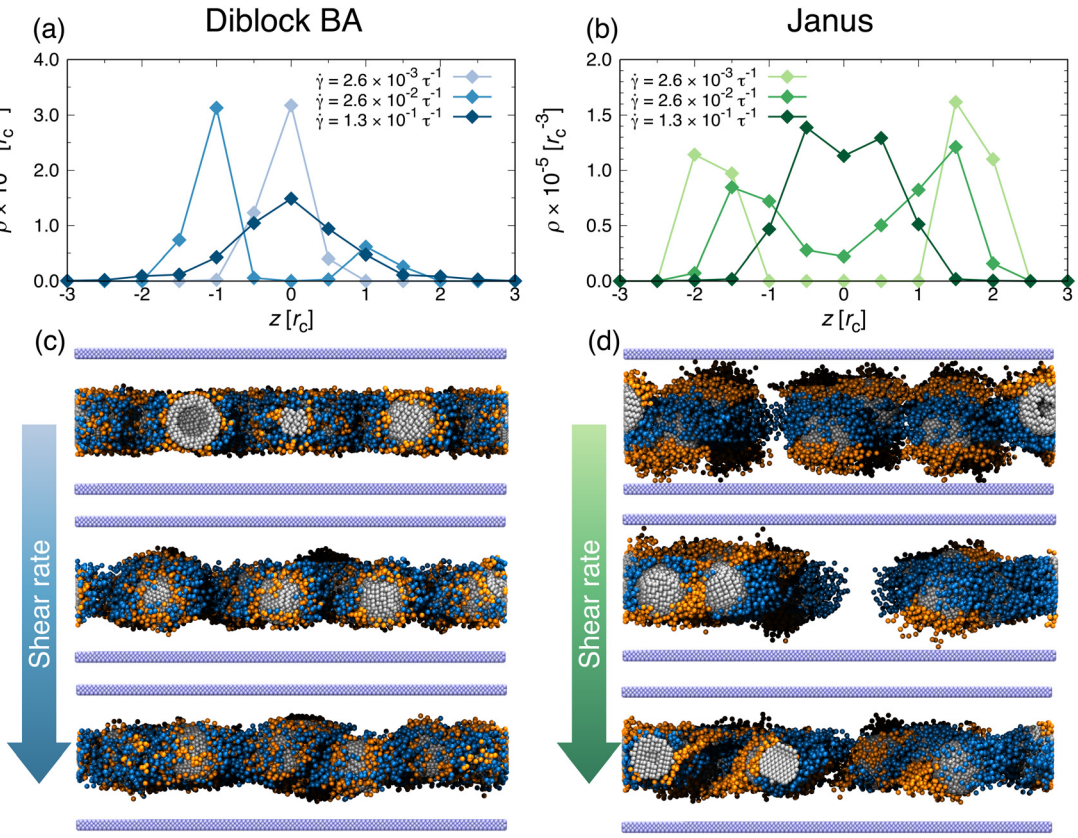

Fig. 10 Density profiles of centers-of-mass of NPs of (a) diblock BA- and (b) Janus-type PGNPs along the wall-normal direction under hydrophobic wall brushes for various shear rates $\dot{\gamma}$, as indicated. Side view of (c) diblock BA- and (d) Janus-type PGNPs at the corresponding $\dot{\gamma}$.

low, intermediate, and high $\dot{\gamma}$ values. For the BA-type PGNPs, at a low shear ($\dot{\gamma} = 2.6 \times 10^{-3}\,\tau^{-1}$), the NP distribution exhibited a single central peak at $z = 0\,r_c$. Upon increasing $\dot{\gamma}$ to $2.6 \times 10^{-2}\,\tau^{-1}$, the central peak split into two, and an additional probability appeared closer to the walls (*i.e.*, $|z| \approx 1.0\,r_c$), indicating migration toward the walls. At high shear rates ($\dot{\gamma} = 1.3 \times 10^{-1}\,\tau^{-1}$), the peaks near each wall become markedly broader; as a result, they overlap and appear as a single merged peak in the recentered representation (consistent with the snapshots in Fig. 7(c)). In contrast, the Janus-type PGNPs displayed pronounced near-wall localization at low shear with a reduced central probability compared with that observed for the BA-type PGNPs. Upon increasing $\dot{\gamma}$, the probability in the central region ($-1\,r_c \lesssim z \lesssim 1\,r_c$) became finite (without forming a distinct peak); however, the distribution retained pronounced near-wall localization, yielding a bimodal profile over an extended $\dot{\gamma}$ range. The tribological behaviors shown in Fig. 7(c) and (d) can therefore be rationalized based on the structural changes induced by shear. Under low shear conditions, Janus-type PGNPs residing near the walls produced a solvent-rich central region to yield a low-resistance pathway, resulting in a lower viscosity than the BA-type PGNP system, whose particles occupied the center and impeded the central flow. At intermediate shear, BA-type PGNPs were almost absent from the channel center, thereby producing a solvent-rich core and lowering the viscosity. In contrast, for the Janus-type PGNPs, the NPs were distributed both near the walls and in the central region ($z \approx 0\,r_c$), which narrowed the core pathway and maintained a higher viscosity over the same $\dot{\gamma}$ range. Consequently, the viscosity ordering reversed at intermediate shear ($1.5 \times 10^{-2}\,\tau^{-1} \lesssim \dot{\gamma} \lesssim 6.0 \times 10^{-2}\,\tau^{-1}$) and the BA-type PGNPs became less viscous than the Janus-type structures. At high shear ($\dot{\gamma} \gtrsim 6.0 \times 10^{-2}\,\tau^{-1}$), the Janus-type PGNPs also exhibited distinct shear-thinning behavior, which originated from the shear-induced alignment and breakup of aggregates. Similar shear-induced density modulations perpendicular to the flow, and their sensitivity to small differences in effective interactions, have been reported for related confined-particle systems.[61] In this sense, the trends in Fig. 10 can be viewed as phenomenologically consistent with such observations.

4 Conclusions

Using dissipative particle dynamics, the organization and flow of polymer-grafted nanoparticles (PGNPs) confined between polymer-brushed walls were examined, along with the roles that their grafting architectures play in defining the tribological properties. Specifically, the equilibrium and shear conditions were investigated, along with the affinities to hydrophilic and hydrophobic walls, and three different grafting architectures (AB and BA diblocks and Janus-type structures). In the presence of hydrophilic wall-brushes at equilibrium, the AB-type PGNPs dimerized, whereas the BA- and Janus-type PGNPs remained dispersed. Under shear stress, the friction coefficient (μ) and apparent viscosity (η) exhibited shear-thinning behavior. Architectural differences were limited in this case because the response was governed primarily by the shear-induced alignment of the wall brushes. Consequently, μ and η were similar across the AB-, BA-, and Janus-type architectures. In contrast, under hydrophobic wall-brush conditions, the equilibrium structures diverged. Specifically, the AB-type PGNPs formed network-like aggregates, the BA-type PGNPs remained dispersed, and the Janus-type PGNPs remained dispersed while orienting their hydrophobic hemispheres toward the hydrophobic brushes. Under shear conditions, the values of μ and η were lower than those in the presence of hydrophilic wall-brushes, and the differences among the architectures became prominent. At low shear, the Janus-type PGNPs yielded the lowest μ and η values by occupying the near-wall regions and preserving a solvent-rich channel at the center of the slit. At intermediate shear, crossover occurred, wherein the BA-type PGNPs became less viscous than the Janus-type PGNPs since the former were essentially absent from the channel center, which reopens a low-resistance core pathway, whereas the latter retained a finite center population that constricts this pathway. In the case of high shear conditions, both architectures reconcentrated toward the center under strong alignment, and the differences in μ and η diminished. These findings establish a mechanistic connection between the density redistribution under confinement (wall-adjacent *vs.* central occupancy), the orientational ordering of the PGNPs and the brushes, and the macroscopic dissipation. They also provide practical design guidelines for brush–PGNP lubricants under confinement, wherein Janus architectures should be selected for low-shear operation to maintain a solvent-rich core *via* near-wall occupation, and BA architectures should be selected for intermediate-shear operation to minimize dissipation by clearing the channel center. The propensity of AB-type PGNPs to aggregate under hydrophobic wall-brush conditions indicates that this architecture is less suitable for low-dissipation operations in the present geometry.

Overall, the obtained results indicate that the grafting architecture and wall affinity are the two primary determinants of self-assembly and flow in nanoconfinement. By explicitly linking the grafting architecture, wall affinity, and shear, this framework complements prior maps based on the solvent quality and grafting density, and establishes a basis for the design of next-generation nanolubricants with predictable performances. Future research incorporating polydispersity, wall roughness, electrostatic interactions, and topological constraints associated with polymer entanglements (*e.g.*, using slip-spring or related approaches) could extend the generality of this design rule.

Conflicts of interest

The authors declare no conflict of interest.

Data availability

The data that support the findings of this study are available from the corresponding author upon reasonable request.

Supplementary information (SI) is available. See DOI: https://doi.org/10.1039/d5me00195a.

Acknowledgements

Y. K. acknowledges JSPS KAKENHI Grant No. JP24K17216 and the support of KIT Grants-in-Aid for Early-Career Scientists. T. I. was supported by JSPS KAKENHI Grant No. JP25K23425.

References

1 G. C. Ritsema van Eck, L. Chiappisi and S. de Beer, *ACS Appl. Mater. Interfaces*, 2022, **4**, 3062–3087.
2 C. Tadokoro, D. Kitafuji, T. Nagamine, K. Nakano, S. Sasaki, T. Sato, K. Sakakibara and Y. Tsujii, *Tribol. Lett.*, 2022, **70**, 106.
3 M. A. Abdelbar, J. P. Ewen, D. Dini and S. Angioletti-Uberti, *Biointerphases*, 2023, **18**, 010801.
4 R. Ishraaq and S. Das, *Chem. Commun.*, 2024, **60**, 6093–6129.
5 M. Miyazaki, K. Nakano, C. Tadokoro, S.-C. Vlădescu, T. Reddyhoff, S. Sasaki and Y. Tsujii, *Wear*, 2021, **482–483**, 203984.
6 Z. Ding, C. Chen, Y. Yu and S. de Beer, *J. Mater. Chem. B*, 2022, **10**, 2430–2443.
7 Y. Liu, Y. Wu and F. Zhou, *Langmuir*, 2023, **39**, 37–44.
8 H. Okubo, D. Kagiwata, K. Nakano and Y. Tsujii, *Langmuir*, 2023, **39**, 18458–18465.
9 V. P. Nguyen, P. Q. Phi and S. T. Choi, *ACS Appl. Mater. Interfaces*, 2019, **11**, 11988–11998.
10 W. Lin, N. Kampf and J. Klein, *ACS Nano*, 2020, **14**, 7008–7017.
11 V. Adibnia, Y. Ma, I. Halimi, G. C. Walker, X. Banquy and E. Kumacheva, *ACS Nano*, 2021, **15**, 8953–8964.
12 A. Horechyy, J. Paturej, B. Nandan, D. Jehnichen, M. Göbel, U. Reuter, J.-U. Sommer and M. Stamm, *J. Colloid Interface Sci.*, 2020, **578**, 441–451.
13 Y. Zhou, S. L. L. Bore, A. R. Tao, F. Paesani and G. Arya, *npj Comput. Mater.*, 2023, **9**, 224.
14 B. Li, H. Gao and Z.-Y. Lu, *Nanoscale*, 2023, **15**, 9775–9782.
15 M. Xu, E. J. Kim, Y. J. Lee, H. Lee, K. Jung, J. Choi, S. H. Kim, Y. J. Kim, H. Yun and K. Bumjoon, *Sci. Adv.*, 2024, **10**, eado0745.
16 P. Adhya, S. M. B. Gautham, T. K. Patra, M. Kaushal and T. Mondal, *Soft Matter*, 2025, **21**, 4156–4164.
17 C. Koh, G. S. Grest and S. K. Kumar, *ACS Nano*, 2020, **14**, 13491–13499.
18 A. Kim, T. Vo, H. An, P. Banerjee, L. Yao, S. Zhou, C. Kim, D. J. Milliron, S. C. Glotzer and Q. Chen, *Nat. Commun.*, 2022, **13**, 6774.
19 L. Jiang, X. Mao, C. Liu, X. Guo, R. Deng and J. Zhu, *Chem. Commun.*, 2023, **59**, 14223–14235.
20 M. Borówko, T. Staszewski and J. Tomasik, *J. Phys. Chem. B*, 2023, **127**, 5150–5161.
21 P.-L. Zhang, B. Li and Z.-Y. Sun, *J. Chem. Phys.*, 2025, **163**, 134903.
22 C. A. Miller and M. J. A. Hore, *ACS Polym. Au*, 2021, **2**, 157–168.
23 J. C. Conrad and M. L. Robertson, *JACS Au*, 2023, **3**, 333–343.
24 B. Li, H. Gao and Z.-Y. Lu, *et al.*, *Nanoscale*, 2023, **15**, 9775–9782.
25 C. Inada, Y. Kobayashi, M. Yamakawa and A. Kitagawa, *Colloids Surf., A*, 2024, **692**, 133921.
26 J. Midya and A. Nikoubashman, *Macromolecules*, 2025, **58**, 10267–10275.
27 S.-T. Wang, H. Zhang, S. Xuan, D. Nykypanchuk, Y. Zhang, G. Freychet, B. M. Ocko, R. N. Zuckermann, N. Todorova and O. Gang, *J. Am. Chem. Soc.*, 2022, **144**, 8138–8152.
28 A. Kim, S. Lee, J. Park, D. J. Smith and M. Cho, *Nat. Commun.*, 2022, **13**, 4827.
29 A. M. Wong, K. Je, C. Y. Zheng, L. Jibril, Z. Miao, S. C. Glotzer and C. A. Mirkin, *Nano Lett.*, 2023, **23**, 116–123.
30 Y. Zhang, H. Tang, R. Wang and L. Zhang, *Macromolecules*, 2023, **56**, 1189–1198.
31 S. Burgess, K. P. Santo, Y. Brun and A. V. Neimark, *J. Phys. Chem. C*, 2020, **124**, 1478–1483.
32 T. Sato, Y. Kobayashi, T. Michioka and N. Arai, *Soft Matter*, 2021, **17**, 4047–4058.
33 T. Sato, Y. Kobayashi and N. Arai, *J. Phys.: Condens. Matter*, 2021, **33**, 365404.
34 M. Borówko and T. Staszewski, *Int. J. Mol. Sci.*, 2022, **23**, 7919.
35 L. B. Krott, T. Puccinelli and J. R. Bordin, *Soft Matter*, 2024, **20**, 4681–4691.
36 A. Steinhaus, T. Pelras, R. Chakroun, A. H. Groschel and M. Mullner, *Macromolecules*, 2018, **51**, 1423–1432.
37 J. Singh, S. Gupta and P. Chokshi, *Soft Matter*, 2024, **20**, 1543–1553.
38 P. Hoogerbrugge and J. Koelman, *Europhys. Lett.*, 1992, **19**, 155–160.
39 P. Español and P. Warren, *Europhys. Lett.*, 1995, **30**, 191–196.
40 R. D. Groot and P. Warren, *J. Chem. Phys.*, 1997, **107**, 4423–4435.
41 S. Biagi, L. Rovigatti, M. Abbasi, L. Bureau, F. Sciortino and C. Misbah, *Soft Matter*, 2021, **17**, 9235–9245.
42 R. G. M. Badr, L. Hauer, D. Vollmer and F. Schmid, *Langmuir*, 2024, **40**, 12368–12380.
43 V. Arya and C. Bakli, *Nanoscale*, 2025, **17**, 19854–19869.
44 X. Deng and F. Muller-Plathe, *Langmuir*, 2025, **41**, 14287–14299.
45 R. Groot and K. Rabone, *Biophys. J.*, 2001, **81**, 725–736.
46 T. Morioka, Y. Kobayashi, T. Ikeda and M. Yamakawa, *Langmuir*, 2025, **41**, 18092–18101.
47 H. Kamberaj, R. J. Low and M. P. Neal, *J. Chem. Phys.*, 2005, **122**, 224114.
48 Y. Kobayashi and N. Arai, *Langmuir*, 2017, **33**, 736–743.
49 M. Inutsuka, N. L. Yamada, K. Ito and H. Yokoyama, *ACS Macro Lett.*, 2013, **2**, 265–268.
50 T. Zhou, H. Qi, L. Han, D. Barbash and C. Y. Li, *Nat. Commun.*, 2016, **7**, 11119.

51 Y. Kobayashi, K. Nomura, T. Kaneko and N. Arai, *J. Phys.: Condens. Matter*, 2020, **32**, 115901.
52 W. M. Brown, P. Wang, S. J. Plimpton and A. N. Tharrington, *Comput. Phys. Commun.*, 2011, **182**, 898–911.
53 S. Plimpton, *J. Comput. Phys.*, 1995, **117**, 1–19.
54 R. B. Thompson, V. V. Ginzburg, M. W. Matsen and A. C. Balazs, *Science*, 2001, **292**, 2469–2472.
55 M. R. Bockstaller, Y. Lapetnikov, S. Margel and E. L. Thomas, *J. Am. Chem. Soc.*, 2003, **125**, 5276–5277.
56 Y. Kobayashi, N. Arai and A. Nikoubashman, *Soft Matter*, 2020, **16**, 476–486.
57 E. Bianchi, A. Z. Panagiotopoulos and A. Nikoubashman, *Soft Matter*, 2015, **11**, 3767–3771.
58 R. A. DeLaCruz-Araujo, D. J. Beltran-Villegas, R. G. Larson and U. M. Cordova-Figueroa, *Soft Matter*, 2016, **12**, 4071–4081.
59 Y. Kobayashi, N. Arai and A. Nikoubashman, *Langmuir*, 2020, **36**, 14214–14223.
60 D. Irfachsyad, D. Tildesley and P. Malfreyt, *Phys. Chem. Chem. Phys.*, 2002, **4**, 3008–3015.
61 A. Scacchi and J. F. Brady, *Phys. Rev. Res.*, 2020, **2**, 032064.